The Astrophysical Journal, 874:40 (13pp), 2019 March 20 https://doi.org/10.3847/1538-4357/ab0085

Dancing in the Dark: Uncertainty in Ultrafaint Dwarf Galaxy Predictions from Cosmological Simulations

Ferah Munshi[1,2,3], Alyson M. Brooks[3], Charlotte Christensen[4], Elaad Applebaum[3], Kelly Holley-Bockelmann[2], Thomas R. Quinn[5], and James Wadsley[6]
[1] Department of Physics & Astronomy, University of Oklahoma, 440 W. Brooks St., Norman, OK 73019, USA
[2] Department of Physics & Astronomy, Vanderbilt University, 6301 Stevenson Center, Vanderbilt University, Nashville, TN 37235, USA
[3] Department of Physics & Astronomy, Rutgers, The State University of New Jersey, 136 Frelinghuysen Rd., Piscataway, NJ 08854, USA
[4] Department of Physics & Astronomy, Grinnell University, Grinnell, IA 50112, USA
[5] Department of Astronomy, University of Washington, 3910 15th Ave., Seattle, WA 98195, USA
[6] Department of Physics & Astronomy, McMaster University, Hamilton, ON L8S 4K1, Canada
Received 2018 October 26; revised 2019 January 14; accepted 2019 January 19; published 2019 March 19

Abstract

The existence of ultrafaint dwarf (UFD) galaxies highlights the need to push our theoretical understanding of galaxies to extremely low mass. We examine the formation of UFDs by twice running a fully cosmological simulation of dwarf galaxies, but varying star formation. One run uses a temperature–density threshold for star formation, while the other uses an H_2-based subgrid star formation model. The total number of dwarf galaxies that form is different by a factor of 2 between the two runs, but most of these are satellites, leading to a factor of 5 difference in the number of luminous UFD companions around more massive, isolated dwarfs. The first run yields a 47% chance of finding a satellite around an $M_{\rm halo} \sim 10^{10}\,M_{\odot}$ host, while the H_2 run predicts only a 16% chance. Metallicity is the primary physical parameter that creates this difference. As metallicity decreases, the formation of H_2 is slowed and relegated to higher-density material. Thus, our H_2 run is unable to form many (and often, any) stars before reionization removes gas. These results emphasize that predictions for UFD properties made using hydrodynamic simulations, in particular regarding the frequency of satellites around dwarf galaxies, the slope of the stellar mass function at low masses, and the properties of ultrafaint galaxies occupying the smallest halos, are extremely sensitive to the subgrid physics of star formation contained within the simulation. However, upcoming discoveries of UFDs will provide invaluable constraining power on the physics of the first star formation.

Key words: galaxies: dwarf – galaxies: star formation

1. Introduction

How do galaxies populate low-mass dark matter halos? Is there a lower limit to the halo mass that can form a galaxy? The lowest-mass galaxies that we have observed are the ultrafaint dwarf (UFD) galaxies, which are typically defined to have $M_{\rm star} \lesssim 10^5\,M_{\odot}$. The lowest-mass galaxy yet observed contains only a few hundreds of solar mass in stars (Homma et al. 2018). To understand these extremely low mass systems, a few authors have simulated the formation of isolated UFD galaxies at high resolution (Read et al. 2016; Jeon et al. 2017; Corlies et al. 2018). Some cosmological simulations of classical dwarf galaxies have been able to resolve the formation of UFD satellite companions (Wheeler et al. 2015, 2018; Munshi et al. 2017). In general, fully cosmological simulations of more massive galaxies like the Milky Way have not had sufficient resolution to resolve the formation of UFD companions, preventing direct predictions for UFD abundances and distributions that can be tested with the Large Synoptic Survey Telescope (LSST; Tollerud et al. 2008; Walsh et al. 2009). However, the next generation of cosmological simulations will achieve stellar mass resolutions of $\sim$1000 $M_{\odot}$, allowing simulators to start pushing down into the UFD range. In this paper, we explore whether the prescriptions commonly adopted by simulators to create realistic Milky-Way-mass and classical dwarf galaxies can be extrapolated down to UFD scales and the impact of prescription choice on observational predictions made using cosmological simulations.

Cosmological simulations of galaxies run to $z = 0$ have recently been quite successful in matching a long list of observed scaling relations (Governato et al. 2010, 2012; Brook et al. 2012; Aumer et al. 2013; Munshi et al. 2013; Vogelsberger et al. 2013; Brooks & Zolotov 2014; Hopkins et al. 2014; Shen et al. 2014; Schaye et al. 2015; Wang et al. 2015; Christensen et al. 2016; Sawala et al. 2016; Garrison-Kimmel et al. 2018; Nelson et al. 2018; Santos-Santos et al. 2018). This success is despite the fact that different simulators often adopt different physical prescriptions, particularly the prescriptions for star formation and energetic feedback from stars, supernovae, and active galactic nuclei. It is generally agreed that different simulators can broadly reproduce the same observed trends despite different prescriptions because galaxies "self-regulate," i.e., a change in the star formation prescription is counterbalanced by subsequent feedback (Saitoh et al. 2008; Hopkins et al. 2011, 2013, 2018; Christensen et al. 2014b; Benincasa et al. 2016; Pallottini et al. 2017). Previous studies found that self-regulation can occur as long as the resolution is high enough to capture the average densities in giant molecular clouds (GMCs), and therefore that the simulation has high enough resolution to have star formation limited to the scales of GMCs (Agertz & Kravtsov 2016; Semenov et al. 2016; Buck et al. 2018).

Semenov et al. (2018) show that self-regulation is limited to the regime of strong feedback, which regulates the gas supply available to turn into stars. Star formation efficiency drops as halo mass decreases, so it is not clear that UFDs lie in the regime of strong feedback, or have the ability to self-regulate. In fact, some simulators have shown that low-mass halos can completely shut off their own star formation via feedback (e.g.,

Fitts et al. 2017; Wright et al. 2019). UFDs are also thought to reside in halos that are susceptible to heating from the UV background, which cuts off gas accretion to the galaxy, removing fuel for star formation (e.g., Brown et al. 2014; Weisz et al. 2014a; Oñorbe et al. 2015; Wheeler et al. 2015). Taken together, these processes suggest that UFDs cannot self-regulate. Thus, the choice of prescriptions for star formation and feedback in cosmological simulations may strongly affect their resulting stellar mass, unlike in more massive galaxies. In this paper we isolate the effect of star formation prescriptions that vary across simulations in terms of both the details of the simulation and the consequences for observational predictions.

One of the key differences in star formation recipes between cosmological galaxy simulations is the threshold mass density at which star formation is allowed to occur. By definition, lower-resolution simulations do not have the ability to resolve high-density gas peaks. Thus, the density threshold must vary with resolution of the simulation. Star formation density thresholds vary from $\sim 1\, m_{\rm H}\,{\rm cm}^{-3}$, where $m_{\rm H}$ is the mass of a hydrogen atom in grams, in lower-resolution simulations (e.g., APOSTLE; Fattahi et al. 2016) to $10\, m_{\rm H}\,{\rm cm}^{-3}$ (e.g., NIHAO; Wang et al. 2015) to $>100\, m_{\rm H}\,{\rm cm}^{-3}$ (e.g., Governato et al. 2010; Shen et al. 2014; Hopkins et al. 2014, 2018; Read et al. 2016). A maximum temperature threshold for star formation is also usually applied. Many simulations adopt a temperature cap of $\sim 10^4$ K because this is the peak of the cooling curve and gas is expected to rapidly cool to lower temperatures (see, e.g., Saitoh et al. 2008).

Beyond this temperature–density model, some simulators also track the presence of molecular hydrogen, H_2, requiring that it be present in order to form stars. The H_2-based star formation models broadly break down into two categories, equilibrium (Krumholz et al. 2008, 2009; Kuhlen et al. 2012; Hopkins et al. 2014, 2018) or nonequilibrium (Robertson & Kravtsov 2008; Gnedin et al. 2009; Gnedin & Kravtsov 2010, 2011; Christensen et al. 2012). Both models, by requiring the presence of H_2, ensure that stars form from high-density gas: generally star formation occurs in gas with $n > 100\, m_{\rm H}\,{\rm cm}^{-3}$, but it can be as high as $n > 1000\, m_{\rm H}\,{\rm cm}^{-3}$ depending on metallicity and resolution. The temperature cap for star formation is also usually lowered in these models as additional cooling processes are captured. The equilibrium models do not explicitly track the formation and destruction of H_2, but rather assume a two-phase interstellar medium in which formation and destruction are balanced. In the nonequilibrium model, the formation and destruction of H_2 are instead explicitly followed. Thus, in the nonequilibrium models, star formation is dependent on the timescale of H_2 formation, which is not the case in the equilibrium models.

Using an equilibrium H_2 model, Kuhlen et al. (2012) showed that an H_2-based star formation prescription could dramatically suppress star formation in low-mass halos where metallicities are low (and thus H_2 is unable to form). However, the suppression is weakened in H_2 formation models if dense gas is able to shield and form H_2 despite low metallicities when sufficiently high resolutions are achieved (e.g., Hopkins et al. 2013). In this paper, we show that adopting a nonequilibrium model leads to further changes. At low metallicities, there is a delay in H_2 formation times in nonequilibrium models, leading to a quantitative difference in the ability of UFD galaxies to form stars compared to temperature–density threshold models.

The two star formation prescriptions that we explore in this paper were also adopted in Christensen et al. (2014b; "Metals" and "H_2" in that work), where it was shown that both models produce dwarf galaxies with nearly identical structural parameters (rotation curves, dark matter density profiles, baryonic angular momentum distributions) for galaxies with $\sim 10^8\, M_\odot$ in stellar mass. Only the mass in galactic winds varied, but by less than a factor of two. We show in this work that, although these star formation prescriptions lead to similar galaxies in the classical dwarf galaxy mass range, differences arise on the scale of UFDs.

The differences that star formation prescriptions introduce on UFD scales have important ramifications, e.g., for the slope and scatter at the faint end of the stellar mass–halo mass (SMHM) relation and the slope of the stellar mass function (SMF) in the ultrafaint regime (Lin & Ishak 2016; Munshi et al. 2017). In this paper we also emphasize the impact on the expected number of UFD satellites in dwarf galaxies, as this has been an active area of investigation recently (Wheeler et al. 2015; Dooley et al. 2017b), particularly with respect to possible companions of the Magellanic Clouds (Deason et al. 2015; Yozin & Bekki 2015; Jethwa et al. 2016; Dooley et al. 2017a; Sales et al. 2017; Kallivayalil et al. 2018; Li et al. 2018). The favored Λ cold dark matter (ΛCDM) cosmological model predicts that structure formation is self-similar. All dark matter halos should contain an abundance of dark matter substructure, from the largest galaxy cluster halos to the smallest halos containing observed dwarf galaxies, and beyond. The scale-free nature of the subhalo mass function in ΛCDM suggests that groups of subhalos should be common (D'Onghia & Lake 2008; Li & Helmi 2008; Nichols et al. 2011; Sales et al. 2011). Because low-mass halos form earlier, are denser, and fall into smaller hosts before larger ones, it is likely that satellites of satellites or of low-mass isolated halos have survived longer than their counterparts that fell directly into the Milky Way (Diemand et al. 2005). This suggests that one way to search for ultrafaint galaxies might be to search for satellites of known dwarf galaxies (Rashkov et al. 2012; Sales et al. 2013; Wheeler et al. 2015; Carlin et al. 2016; Patel et al. 2018). Dooley et al. (2017b) used a range of SMHM relations derived from abundance matching results combined with a model for reionization to show that isolated dwarfs in the Local Group are extremely interesting targets in the hunt for ever-fainter dwarfs.

This paper is organized as follows: We describe our simulations in Section 2. In Section 3 we quantify the occupation fraction of dark matter halos as a function of declining halo mass and show that at the lowest halo masses there is a drastic difference in the number of luminous dwarf galaxy satellites in simulations with different star formation prescriptions. We find that the inability of low-mass halos to form H_2 in the reionization epoch suppresses star formation relative to the same halos run with a temperature–density threshold star formation model. In Section 4, we demonstrate how the choice of star formation implementation impacts various quantities (star formation histories [SFHs], SMF, and probability of a classical dwarf hosting UFD satellites) that have recently been studied using simulations of dwarf galaxies. We discuss our results, including limitations of our model, in Section 5. We summarize in Section 6.

2. The Simulations

The simulations used in this work are run with the *N*-Body + smoothed particle hydrodynamics (SPH) code CHANGA (Menon et al. 2015) in a fully cosmological ΛCDM context using *Wilkinson Microwave Anisotropy Probe* Year 3 cosmology: $\Omega_0 = 0.26$, $\Lambda = 0.74$, $h = 0.73$, $\sigma_8 = 0.77$, $n = 0.96$. CHANGA utilizes the CHARM++ run-time system for dynamic load balancing and computation/communication overlap in order to effectively scale up the number of cores. This improved scaling has allowed for the simulation of large, high-resolution volumes (e.g., Anderson et al. 2017; Tremmel et al. 2017) that were previously unattainable with CHANGA's predecessor code, GASOLINE. We use this scaling here to simulate a volume of dwarf galaxies, twice, requiring a total of ∼10 million CPU hours.

CHANGA adopts all the same physics modules (described below) as GASOLINE but has an improved SPH implementation that uses the geometric mean density to more realistically model the gas physics at the hot–cold interface (Wadsley et al. 2017). The developers of CHANGA are part of the AGORA Collaboration, which aims to compare the implementation of hydrodynamics across cosmological codes (Kim et al. 2014, 2016).

Our galaxy sample is drawn from a uniform dark-matter-only simulation of a cube with 25 Mpc per side. From this volume, we select a field-like region representing a cosmological "sheet" roughly 3 Mpc in diameter, containing almost 7000 isolated dark matter halos from $2 \times 10^{10}\,M_\odot$ in halo mass down to our resolution limit of $4.3 \times 10^5\,M_\odot$ (64 particles). We then resimulate this field at extremely high resolution using the "zoom-in" volume renormalization technique (Katz & White 1993). The zoom-in technique allows for high resolution in the region of interest, while accurately capturing the tidal torques from large-scale structure that deliver angular momentum to galaxy halos (Barnes & Efstathiou 1987). These zoom-in simulations have a hydrodynamical smoothing length as small as 6 pc, a gravitational force softening of 60 pc, and an equivalent resolution to a 4096^3 particle grid. Dark matter particles have a mass of $6650\,M_\odot$, while gas particles begin with a mass of $1410\,M_\odot$, and star particles are born with 30% of their parent gas particle mass. The dark-matter-only version of this volume was run in both a CDM and self-interacting dark matter model in Fry et al. (2015). Following the convention in that paper, we adopt the nickname "The 40 Thieves."

Metal Cooling (MC): The "Metal Cooling (MC)" version of the 40 Thieves includes cooling of the gas via primordial and metal-line cooling, nonequilibrium abundances of H and He, and diffusion of metals to neighboring gas particles (Shen et al. 2010). Additionally, we adopt a simple model for self-shielding of the H I gas following Pontzen et al. (2008). Star formation occurs stochastically when gas particles become cold ($T < 10^4$ K) and when gas reaches a density threshold of $100\,m_{\rm H}\,{\rm cm}^{-3}$, comparable to the mean density of molecular clouds. The probability, p, of spawning a star particle is a function of the local dynamical time $t_{\rm form}$:

$$p = \frac{m_{\rm gas}}{m_{\rm star}}(1 - e^{-c^*\Delta t/t_{\rm form}}), \quad (1)$$

where $m_{\rm gas}$ is the mass of the gas particle and $m_{\rm star}$ is the initial mass of the potential star particle. A star formation efficiency parameter, $c^* = 0.1$, gives the correct normalization of the Kennicutt–Schmidt relation (Christensen et al. 2014b).

Molecular Hydrogen (H_2): The "Molecular Hydrogen (H_2)" version of the 40 Thieves includes the aforementioned metal-line cooling and metal diffusion, with the addition of nonequilibrium H_2 abundances and H_2-based star formation. Our H_2 abundance calculation includes both a gas-phase and dust-dependent description of H_2 creation and destruction. H_2 forms via H^- in the gas phase and is collisionally dissociated. The dust phase is dominant as soon as a small amount of metals are present. A detailed discussion of the calculation of H_2 formation on dust grains is given in Christensen et al. (2012, hereafter CH12). Destruction of H_2 by Lyman–Werner (LW) radiation is calculated owing to both the UV background and nearby young stars. An extensive calculation of the photodissociation by LW radiation is found in CH12. Shielding of H I and H_2 is based on particle metallicity (Gnedin et al. 2009, CH12). As in CH12, the SFR in this simulation is set by the local gas density and the H_2 fraction. The star formation probability is again given by Equation (1), but c^* is modified such that $c^* = c_0^* X_{\rm H_2}$, where $c_0^* = 0.1$ and $X_{\rm H_2}$ is the fraction of baryons in H_2. We restrict star formation to occur in gas particles with $T < 10^3$ K. With the inclusion of the H_2 fraction term, gas in low-metallicity dwarfs tends to reach even higher densities (required for the gas to shield and form H_2) than the MC model before it can form stars (Christensen et al. 2014b).

We apply a uniform, time-dependent UV field from Haardt & Madau (2012) to model photoionization and photoheating for both runs. Both simulations adopt the "blast wave" supernova feedback approach (Stinson et al. 2006), in which mass, thermal energy, and metals are deposited into nearby gas when massive stars evolve into supernovae. The thermal energy deposited among those nearby gas neighbors is 10^{51} erg per supernova event. Following Stinson et al. (2010), we quantize the feedback so that supernovae only occur when whole stars have gone supernova, as opposed to slowly releasing fractions of supernova energy at every time step. Subsequently, gas cooling is turned off until the end of the momentum-conserving phase of the supernova blast wave. This model keeps gas hydrodynamically coupled at all times.

Our feedback model does not explicitly include processes such as cosmic rays, or those caused by young stars such as photoionization, momentum injection from stellar winds, and radiation pressure (e.g., Thompson et al. 2005; Murray et al. 2011; Hopkins et al. 2012; Sharma & Nath 2012; Wise et al. 2012; Agertz et al. 2013; Booth et al. 2013; Salem et al. 2016; Simpson et al. 2016; Farber et al. 2018; Kannan et al. 2018). However, the physical prescriptions described above have been able to reproduce and explain properties of galaxies over a wide range of masses, regardless of which SF recipe is adopted. In addition to simulating the first bulgeless disk galaxy and dark matter cores (Governato et al. 2010; Brook et al. 2011), simulated galaxies match the observed mass–metallicity relation (Brooks et al. 2007; Christensen et al. 2016), the baryonic Tully–Fisher relation (Christensen et al. 2016; Brooks et al. 2017), the size–luminosity relation (Brooks et al. 2011), the SMHM relation determined from abundance matching (Munshi et al. 2013), and the sizes and fractions of H I in local galaxies (Brooks et al. 2017). They also match the abundance of DLA systems (Pontzen et al. 2008), and the numbers and internal velocities of dwarf spheroidal satellites (Brooks & Zolotov 2014). In what follows, we extend these successful models to lower masses and demonstrate for the first time that

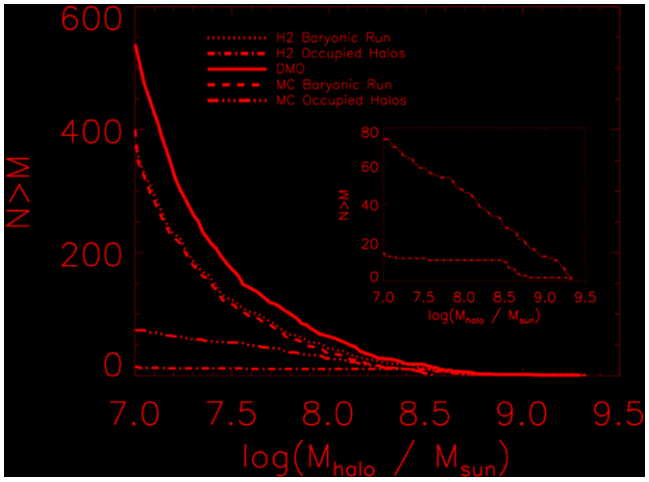

Figure 1. Cumulative halo mass functions. The solid line is the cumulative mass function for the dark-matter-only (DMO) run; the dashed and dotted lines are the cumulative mass function for the two baryonic runs using all halos; the two dot-dashed lines are the cumulative mass function using only occupied (luminous) halos in the baryonic runs. Inset: zoom-in of the occupied halos in both the H_2 and MC runs. The fraction of dark (nonluminous) halos continues to increase with decreasing halo mass in the MC run but remains constant in the H_2 run below $\sim 10^{8.5}\,M_\odot$ in halo mass. The H_2 run contains far fewer occupied halos than the corresponding MC run, by roughly a factor of five.

the differing star formation models impact galaxy formation on UFD scales.

Halos are identified and tracked with Amiga's Halo Finder (AHF Gill et al. 2004; Knollmann & Knebe 2009). AHF calculates the virial mass of each halo (given in this paper by $M_{\rm halo}$) as the total mass with a sphere that encloses an overdensity relative to the critical density of $200\rho_{\rm crit}(z)$.

3. Results

Figure 1 shows the cumulative halo mass functions for both of the baryonic (MC and H_2) and dark-matter-only versions of the 40 Thieves. The top three lines (solid, dashed, and dotted) include all dark matter halos (both isolated and satellite galaxies) down to $10^7\,M_\odot$ in halo mass (corresponding roughly to the hydrogen cooling limit) at $z = 0$, regardless of whether they contain stars. The bottom two lines are only those halos that are "occupied" by stars, and they are also shown separately in an inset for clarity. A given dark matter halo in a baryonic run is less massive than in the corresponding dark-matter-only simulation (see also Munshi et al. 2013; Sawala et al. 2013). The root cause of this mismatch is baryon ejection from low-mass halos (by heating from the UV background and/or as a result of supernova feedback), which slows not only the galaxy growth rate but also the dark matter halo growth rate. As a direct result, the total number of dark matter halos with $M_{\rm halo} > 10^7\,M_\odot$ is reduced ($\sim$75%) in the baryonic versions compared to the dark-matter-only run.

The inset of Figure 1 shows in closer detail the cumulative halo mass function for only those halos that "host a galaxy," i.e., contain a minimum of one star particle (see also Sawala et al. 2015) in both the MC and H_2 runs. The number of luminous halos continues to rise toward lower halo masses in the MC run, but stops rising below $M_{\rm halo} \sim 10^{8.5}\,M_\odot$ in the H_2 run. There are nearly five times as many occupied halos above $10^7\,M_\odot$ in the MC run than in the H_2 run. If we focus only on the higher-mass halos in our matched sample (defined next), the difference drops to about a factor of two (see Figures 2 and 3).

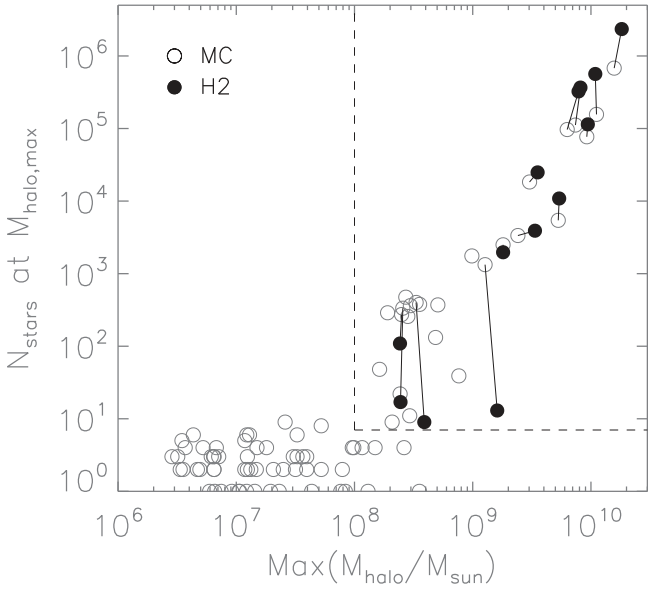

Figure 2. Number of stars in a halo at the time the maximum halo mass is attained vs. the maximum halo mass, for both the MC and H_2 runs. The dashed line separates the galaxies in our matched sample ($M_{\rm halo} > 10^8\,M_\odot$ and $\geqslant$7 star particles). Lines connect matched galaxies in both the MC and H_2 runs. Above $10^9\,M_\odot$ in halo masses, the galaxies are well matched across runs, but below $10^9\,M_\odot$ there are more galaxies produced in the MC run than the H_2 run.

3.1. Matched Sample

The galaxies with one star particles are, by definition, not resolved. In this section we set out to identify a set of halos that can be reliably compared against each other from each run. For every dark matter halo that contains a star particle at $z = 0$, we trace back the most massive progenitor halo and identify the time step in which it has the maximum number of dark matter particles. In Figure 2 we show the halo mass and number of star particles inside the halo at that step. Solid lines connect matched galaxies across the MC and H_2 versions of the simulation. For halos above $10^9\,M_\odot$, halos are well matched, with a one-to-one correspondence between formed galaxies. Below $10^9\,M_\odot$, however, it is clear that the MC run forms more galaxies than the H_2 run, and even in the matched cases the H_2 galaxies tend to form fewer stars at these low halo masses.

For halos with maximum halo mass above $10^8\,M_\odot$ and $N_{\rm star} \geqslant 7$, there are MC halos that contain galaxies but with matched counterparts in the H_2 run that are completely dark. We have examined those dark halos in more detail to test whether their lack of star formation is expected for the H_2 model given the resolution. We have approached this in two ways. First, similar to Kuhlen et al. (2013), we compare the surface densities of our gas particles to the critical surface density $\Sigma_{\rm crit}$ at which atomic H converts to molecular H. The metallicity of our non-star-forming gas is $Z/Z_\odot = 10^{-3}$ or lower. At $Z/Z_\odot = 10^{-3}$, $\Sigma_{\rm crit} = 5700\,M_\odot\,{\rm pc}^{-2}$. The non-star-forming gas in the dark matched H_2 halos remains at surface densities $<10\,M_\odot\,{\rm pc}^{-2}$. Thus, it would not be capable of forming H_2 and therefore should not form stars in the H_2 run (see also Sternberg et al. 2014).

Second, we can examine the timescale, $t_{\rm H_2}$, for atomic H to convert to molecular H following Krumholz (2012). Following

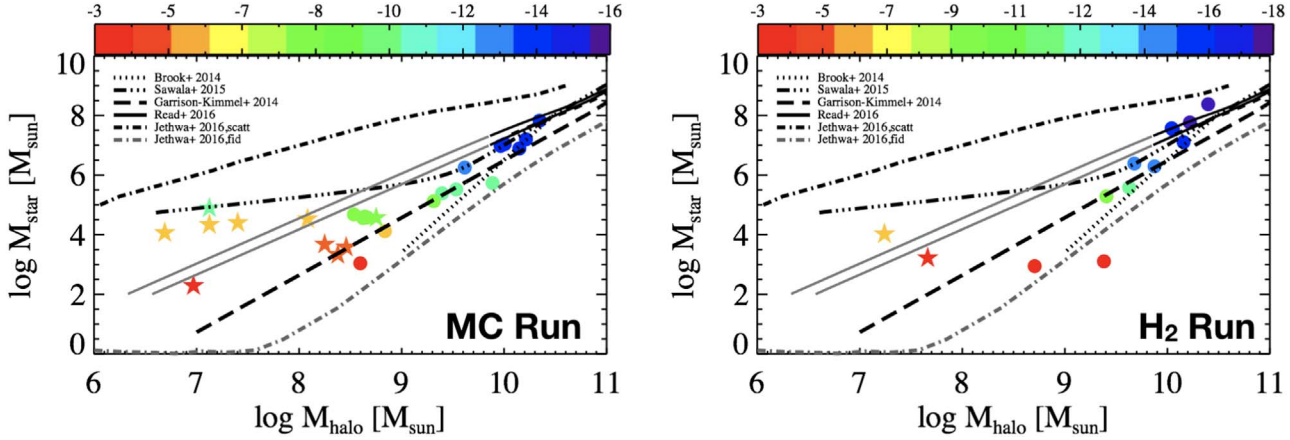

Figure 3. SMHM relationship for both simulations, showing only the matched galaxies from Figure 2. Left panel: MC Run. Right panel: H_2 run. Circles are central galaxies, and stars are resolved satellites. Galaxies are color-coded by their *V*-band magnitude (see color bar on top). Stellar masses are derived based on photometric colors, and halo masses are taken from the DM-only version of the run to be consistent with the abundance matching results shown (Brook et al. 2014; Garrison-Kimmel et al. 2014; Read et al. 2017; Jethwa et al. 2018). We plot $z = 0$ halo masses. We also show simulation results from Sawala et al. (2015). A similar number of central galaxies form in both simulations for $M_{\rm halo} > 10^9\,M_\odot$, but more galaxies form in the MC run at lower halo masses, and there are many more luminous satellites in the MC run.

their Equation (7),

$$\frac{t_{\rm H_2}}{t_{\rm ff}} = 24 Z^{-1} C^{-1} n_0^{-1/2}, \quad (2)$$

where $t_{\rm ff}$ is the freefall time, Z is the metallicity of the gas relative to solar, C is a clumping factor equal to 10 in our simulations, and $n_0 = \langle n_{\rm H}\rangle / 1\,{\rm cm}^{-3}$, where $\langle n_{\rm H}\rangle$ is the mean hydrogen density. For the non-star-forming gas in our matched H_2 halos, $\langle n_{\rm H}\rangle$ is about $10\,m_{\rm H}\,{\rm cm}^{-3}$. The freefall time depends on $\langle n_{\rm H}\rangle$ as well and is 13.6 Myr at $10\,m_{\rm H}\,{\rm cm}^{-3}$. The timescale for H_2 formation, $t_{\rm H_2}$, is more than 10 Gyr for our gas with $Z/Z_\odot = 10^{-3}$. Even at higher densities of $\langle n_{\rm H}\rangle = 100\,m_{\rm H}\,{\rm cm}^{-3}$, the timescale for H_2 formation is over 1 Gyr.

Thus, significant amounts of H_2 simply cannot form in these halos before reionization at this resolution (we discuss limitations of the resolution in Section 5). We conclude that our dark halos in the H_2 run are behaving as expected. We therefore restrict the following analysis to matched halos with $M_{\rm halo,max} > 10^8\,M_\odot$ and $N_{\rm stars} \geqslant 7$. It should be clear that we do not mean that these halos are "converged" across the two star formation recipes. The star formation in the two runs in the lowest-mass halos is dramatically different, with the MC run forming stars while matched halos in the H_2 run remain dark. Even when the H_2 run forms stars, there is a discrepancy in stellar mass with the matched halos in the MC run for halos with $M_{\rm halo,max} \lesssim 10^9\,M_\odot$. This is exactly the difference we wish to explore in this work.

3.2. The Formation of Dwarf Galaxies

In Figure 3 we show the resulting SMHM relation for matched halos in both the MC (left panel) and H_2 (right panel) versions of the 40 Thieves. Each galaxy is color-coded by its *V*-band magnitude at $z = 0$. Filled circles are central (isolated) galaxies, while stars are satellite galaxies. Four of the lines show results from abundance matching in dwarf galaxies (Brook et al. 2014; Garrison-Kimmel et al. 2014; Read et al. 2017; Jethwa et al. 2018), and the fifth line shows the simulation results of Sawala et al. (2015). The stellar masses have been calculated following Munshi et al. (2013), based on photometric colors. To be consistent with abundance matching, the halo masses are the mass in the corresponding dark-matter-only run. Note that we plot $z = 0$ halo masses, while the abundance matching results use maximum halo mass. Thus, the satellite results should not be compared directly to the lines (though we note that all satellites must have peak halo masses above $10^8\,M_\odot$ to be included in the sample shown here).

Again, it is immediately obvious from Figure 3 that there are galaxies residing in halos above $M_{\rm halo} \sim 10^9\,M_\odot$ that are produced in both runs. However, below $\sim 10^9\,M_\odot$ the number of galaxies diverges, with twice as many halos containing galaxies in the MC run. We can now see from Figure 3 that many of these low-mass halos are satellites (colored stars). There are five times as many satellites in the MC run than in the H_2 run.

All of the satellites in these runs are in the ultrafaint luminosity range. Like observed UFDs (Brown et al. 2012, 2014; Weisz et al. 2014a, 2014b), they tend to form the bulk of their stars early, with their star formation trickling off soon after reionization (see Figure 5, discussed further below). In Figure 4 we compare the phase diagram for gas that forms stars within the first 1 Gyr of both simulations (i.e., before the end of reionization at $z \sim 6$). Although there is some overlap in the star formation temperatures and densities between the two runs, there is a clear offset in the regions where the majority of stars form. In the MC run (gray points), stars tend to form from gas that spans a range of temperatures (up to 10^4 K) but is near the threshold density ($100\,m_{\rm H}\,{\rm cm}^{-3}$). In the H_2 run (contours and black points), star-forming gas forms from colder, denser gas (<500 K and $\gtrsim 1000\,m_{\rm H}\,{\rm cm}^{-3}$). This difference was also discussed in CH12 (see their Figure 13).

The higher densities that stars form from in the H_2 model are tied directly to the subgrid H_2 formation model. At solar metallicities, the two models form star particles at similar densities, but the models diverge as metallicity decreases. As described in CH12, when metals are present, the formation of H_2 is dominated by formation on dust grains. In the reionization epoch, when metallicities are extremely low, formation may also proceed through gas-phase reactions. However, during the reionizaton epoch, both of these processes

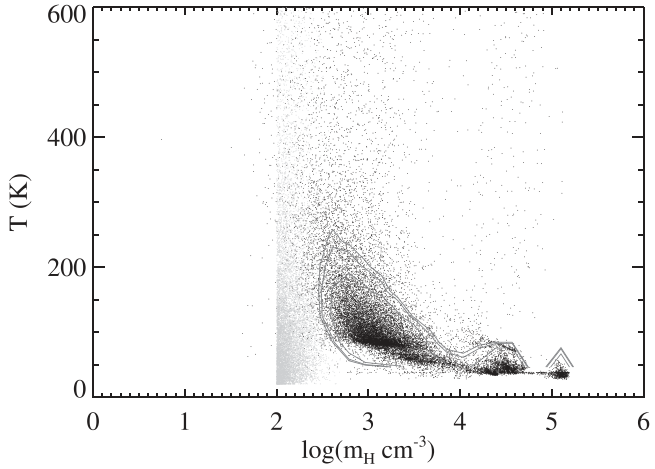

Figure 4. Comparison of the phase diagrams for star-forming gas between the MC run (gray points) and the H_2 run (contours + black points) for all stars formed in the first gigayear of the simulation. Note that the range of densities forming stars in the H_2 run, while slightly overlapping with that in the MC run, overwhelmingly tends to be higher than those in the MC run.

are inefficient and slow. As a result, gas particles will frequently reach high densities through gravitational collapse prior to forming significant amounts of H_2. At the same time, the low metallicities reduce the amount of dust shielding, which means that H_2 (and thus star formation) can only persist in high-density gas. For most of the H_2 subhalos, significant amounts of H_2 can never be created before reionization removes the gas from the halos. In the MC run, because stars can form in lower-density atomic gas, star formation can begin before reionization quenches it. This also explains why the MC run tends to form more stars in general for galaxies in halos with $M_{\rm halo} < 10^9\,M_\odot$ (see Figure 2).

Even at $z = 0$, the most massive matched dwarfs in this work still show a difference in the effective star formation density threshold owing to the impact of metallicity on dust shielding (CH12; Christensen et al. 2014b). Despite this, dwarf galaxies in halos above $\sim 10^9\,M_\odot$ generally still form similar numbers of star particles, due to their ability to self-regulate. This is consistent with the prior results discussed in the Introduction that found that the density threshold had little impact on the resulting SFR. However, a slight excess of stars seems to form in the H_2 model relative to the MC model at these masses (see Figure 2). This excess is likely due to the ability of the gas to shield in the H_2 model, protecting the gas from heating and leading to additional cold gas present in the H_2 simulations. The excess cold gas results in slightly higher stellar masses in the H_2 run in halos of $\sim 10^{10}\,M_\odot$.

Kuhlen et al. (2012) were the first to show that a model for H_2-based star formation could suppress star formation in dwarf galaxies primarily as a result of their lower metallicities. However, they found that their equilibrium H_2 model suppressed all star formation in halos below about $M_{\rm halo} = 10^{10}\,M_\odot$, while our nonequilibrium H_2 model forms stars in halos down to $M_{\rm halo} = 10^{8.5}$. Reionization played no role in Kuhlen et al. (2012), since their lowest-mass halo that was able to form stars was well above the halo mass thought to be impacted by reionization. On the other hand, the changes in stellar mass that we see in halos below $\sim 10^9\,M_\odot$ are explicitly due to the fact that these are halos in which reionization can strongly affect the evolution. The MC halos are able to start forming stars at lower densities than their H_2 counterparts and thus are able to produce more stars before reionization removes their gas.

3.3. Delayed Merging

Early star formation is not the only reason why there are more satellites in the MC run than in the H_2 run: more of the satellites survive. Three of the surviving subhalos in the MC run are completely disrupted in the H_2 run after merging with a parent halo. Two of those halos had managed to form stars in the H_2 run before being fully destroyed. In fact, a close examination of Figure 5 shows that there is a surviving satellite in the MC run with a very extended SFH (thick red dashed line in the left panel). This satellite had a counterpart in the H_2 run with an extended SFH, but the subhalo is completely disrupted and part of the second-largest halo in the H_2 run at $z = 0$. All three of the surviving subhalos in the MC run are completely merged in the dark-matter-only run as well.

Schewtschenko & Macciò (2011) showed that mergers occur later in simulations with baryonic feedback than in matched halos in an identical dark-matter-only simulation. They hypothesized that the pressure of the hot halos found in baryonic simulations slows down accretion of subhalos. Our simulated dwarf galaxies *do* have hot halos of gas around them (Wright et al. 2019), with the mass in hot gas being up to an order of magnitude greater than the H I gas mass. Later infall of subhalos then leads to less tidal mass loss for subhalos simply owing to the fact that there is less time for tidal stripping between infall and $z = 0$ (S. Ahmed et al. 2019, in preparation). The end result should be that fewer satellites are fully destroyed at $z = 0$ for a run with baryonic feedback.[7]

These results suggest that the feedback in the MC run is stronger, delaying mergers of subhalos. Indeed, another indication that feedback is stronger in the MC run is that the overall halo masses tend to be lower (see comparison of maximum $M_{\rm halo}$ for matched halos in Figure 2). As mentioned previously, feedback reduces the growth of halos (Munshi et al. 2013; Sawala et al. 2013). Despite the fact that the feedback recipe is the same in both the MC and H_2 runs, feedback is injected into lower-density gas in the MC run because the MC run rarely reaches the higher densities found in the H_2 run (see, e.g., Figure 7 of Christensen et al. 2014b). When comparing the nine most massive isolated dwarfs at $z = 0$ (where the stellar masses are similar), the H_2 dwarf galaxies on average have 10% higher dark matter mass and more than twice the mass in hot gas within their virial radii (and more baryons generally) compared to their MC counterparts.[8] Thus, it seems that the MC galaxies have been able to remove more baryonic material from their halos, delaying their growth in dark matter as well.

However, this result is seemingly at odds with previous comparisons of these two models (Christensen et al. 2014a), which found that the H_2 model had more effective feedback and drove slightly more outflows. While the previous work used the GASOLINE code, we use ChaNGa with an updated SPH treatment (Wadsley et al. 2017) and quantized feedback. It

[7] This assumes that additional tidal effects from the potential of the central galaxy are negligible. The disk potential is not negligible in Milky-Way-mass galaxies (Peñarrubia et al. 2010; Zolotov et al. 2012; Arraki et al. 2014; Brooks & Zolotov 2014; Garrison-Kimmel et al. 2017b) but is expected to be negligible in dwarf galaxies.

[8] Since the hot gas mass of the MC galaxies is smaller than the H_2 runs, the delayed merging of subhalos does not seem to be a direct result of pressure from the hot halo (as was proposed in Schewtschenko & Macciò 2011), but rather a response to the ejection of the gas itself.

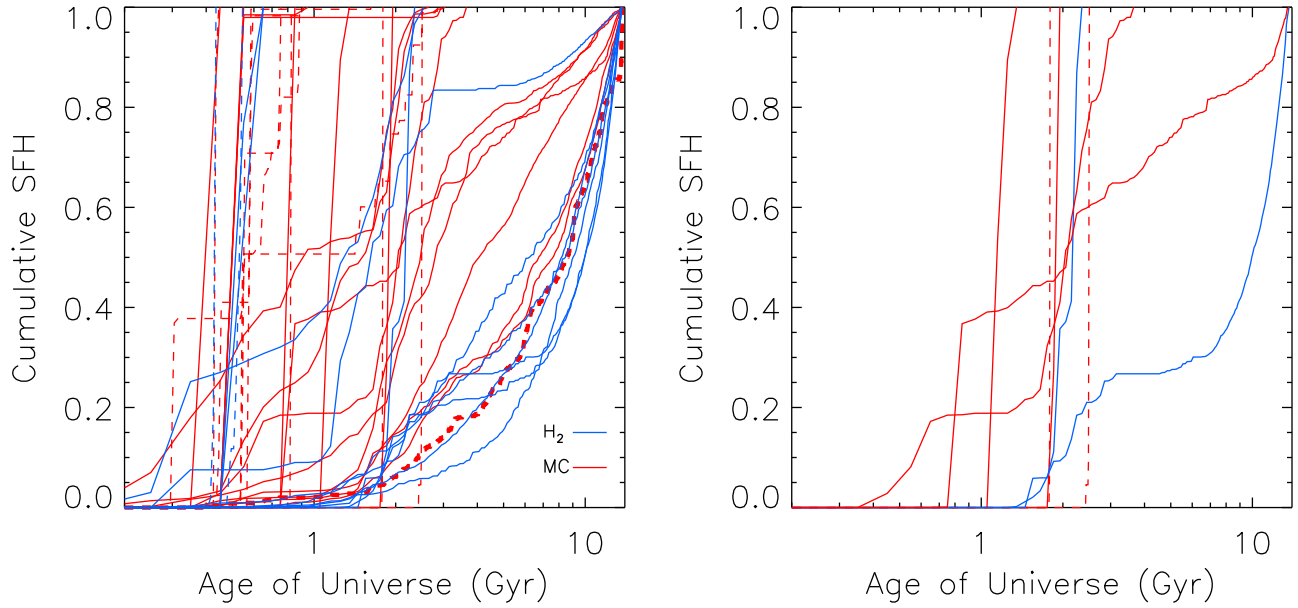

Figure 5. Cumulative SFHs for the simulated galaxies. The MC run is shown in red, the H_2 run in blue. Solid lines are central galaxies at $z = 0$, while dashed lines are satellites. Left panel: all surviving matched galaxies at $z = 0$. One MC satellite is shown in a thicker dashed line that has an extended SFH, but its H_2 counterpart has been destroyed in a merger, as discussed in Section 3.3. Right panel: subset of the galaxies shown in the left panel that are discussed in Sections 3.3 and 4.1. The four MC galaxies that do not begin forming stars until after 1 Gyr are shown (two satellites—red dashed; two centrals—solid red). The two H_2 galaxies that do not start star formation until after 1 Gyr are shown (solid blue) along with their MC counterparts that start forming stars much earlier (solid red).

is not clear whether these changes alter the feedback, making the MC run more effective at removing baryons. A full investigation is beyond the scope of this paper, but we find that all evidence points to stronger feedback in the current MC runs than in the H_2 runs.

In summary, these results suggest that feedback can lead to delayed mergers of the UFD satellites. Combined with the ability to form stars at early times in more halos in the MC run, this makes the difference in satellite numbers even more stark at $z = 0$ between the two runs.

4. Implications

The fact that star formation is restricted to different types of gas in these two commonly adopted models leads to some implications that should be considered when comparing predictions from different simulations. Here we examine a few observables that are commonly predicted by simulators, demonstrating that future observations have the potential to pinpoint more accurate physical models.

4.1. Delayed Star Formation

Consistent with the results presented in Section 3, we find that there is a delay in the onset of star formation in the H_2 run compared to matched halos in the MC run. We highlight a few cases of this in the right panel of Figure 5. In general (as can be seen in the left panel of Figure 5), most of our galaxies begin to form stars before $z = 6$, i.e., in the first 1 Gyr after the big bang. However, there are two (central) galaxies in the H_2 run that only begin to form stars after 1 Gyr (shown in blue). Because their counterparts in the MC run can form stars without first generating significant amounts of H_2, the MC counterparts all begin star formation before the end of reionization (the counterparts are also shown in red in the right panel of Figure 5—they are the two MC galaxies shown that begin star formation before 1 Gyr).

However, post-reionization onset of star formation cannot be attributed to only a single star formation model. There are four galaxies (two centrals and two satellites, shown in the right panel of Figure 5) in the MC run that do not begin to form their stars until after 1 Gyr. In each of the four cases, their counterparts in the H_2 run are dark halos that never formed stars. In that case, we might say that the star formation is so delayed in the H_2 run that it does not occur before $z = 0$.

In general, all observed galaxies have early star formation, though the error bars on the time of onset can be 1 Gyr or more depending on how far down the main-sequence resolved stars are detected (Brown et al. 2012, 2014; Weisz et al. 2014a, 2014b). It is not clear whether our galaxies that delay star formation until after reionization are consistent with observations. However, the dwarf galaxies in these simulated volumes are much farther away from a massive galaxy than any observed galaxies with resolved SFHs that have pushed below the oldest main-sequence turnoff. Our dwarf galaxies are ∼5 Mpc away from a Milky-Way-mass galaxy. It remains to be seen whether environment plays any role in onset of star formation.

In summary, while the H_2 run has consistently later star formation (or none at all by $z = 0$) compared to matched galaxies in the MC run, there is no obvious trend in onset time that could be used to discriminate models based on observations. Rather, it is the number of galaxies and the stellar mass of those galaxies that discriminate the models (discussed in the next section).

4.2. Stellar Mass Function

The factor of two difference in the number of faint dwarf galaxies that form between our two models will lead to different faint ends of the SMF. Additionally, the fact that the MC run forms higher stellar masses for matched galaxies with $M_{\rm halo,max} < 10^9\,M_\odot$ (see Figure 2) will also alter the SMF.

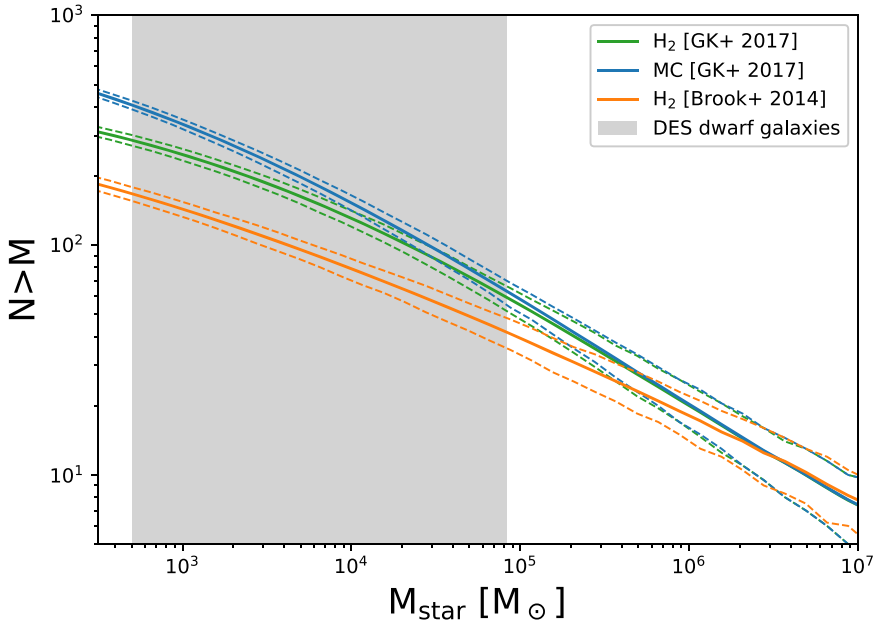

Figure 6. Comparison of SMFs predicted by the H_2 run (green) and the MC run (blue) assuming that the slope and scatter of the SMHM relation follow Garrison-Kimmel et al. (2017a) and following the occupation fractions shown in Figure 1. The orange line is the SMF predicted for the H_2 run assuming that the slope of the SMHM better follows Brook et al. (2014). The gray shaded region represents the recent discovery space for DES. 1σ errors for each mass function are shown in corresponding colored dashed lines.

First, we demonstrate the difference in the SMF that arises owing to the different number of low-mass galaxies in each model alone. For both the MC and H_2 models, we populate an SMF following the method outlined in Garrison-Kimmel et al. (2017a), in which the scatter, σ, in the stellar mass at a given halo mass grows as

$$\sigma = 0.2 + \gamma(\log_{10} M_{\rm halo} - \log_{10} M_1), \quad (3)$$

where γ is the rate at which the scatter grows and M_1 is a characteristic halo mass above which the scatter remains constant. We adopt the scatter model for field galaxies from Garrison-Kimmel et al. (2017a), where $M_1 = 10^{11.5} M_\odot$ and $\gamma = -0.25$. We populate the $z = 0$ ELVIS catalogs (Garrison-Kimmel et al. 2014) with this SMHM relation and then assign galaxies as "dark" based on the fraction of luminous to nonluminous halos shown in Figure 1 for each of our models. The resulting SMFs are shown in Figure 6 as the blue (MC) and green (H_2) lines. We do this 1000 times in order to estimate our errors (dashed lines), and we normalize the results so that each has 12 galaxies with stellar mass comparable to Fornax (this is roughly the number of Fornax-mass galaxies within 1 Mpc; McConnachie 2012). Figure 6 demonstrates that there is a difference in slope below $M_{\rm star} \sim 10^5 M_\odot$, with the H_2 simulation predicting the shallower faint-end slope.

The blue and green lines adopt the same slope and scatter of the SMHM relation and thus only reflect the change in the fraction of "occupied" dark matter halos shown in Figure 1. However, the H_2 model tends to form fewer stars in matched halos at the low-mass end, which will yield a steeper SMHM slope that will impact the SMF. As can be seen in Figure 3, the Garrison-Kimmel et al. (2017a) SMHM slope appears to be a decent fit to the central galaxies in the MC run (left panel). However, the Brook et al. (2014) SMHM slope appears to be a better match to the central galaxies in the H_2 run. Our simulations do not have enough galaxies to independently define the slope and scatter of the SMHM relation for each prescription, so we adopt the slope and scatter of Garrison-Kimmel et al. (2017a) to describe the MC run and those of Brook et al. (2014) to describe the H_2 run, in order to show the additional effect that the steeper SMHM relation will have on the SMF. We assume the same growing scatter as in the Garrison-Kimmel et al. (2017a) relation but applied to the Brook et al. (2014) slope, and again we adopt the galaxy occupation fraction for the H_2 simulation. The result is shown as the orange line in Figure 6. It can now be seen that there is a dramatic difference in the number of expected UFD galaxies in the two models.

The SMF for the two runs is indistinguishable above $M_{\rm star} \sim 10^5 M_\odot$. Since this is the mass range that is currently best constrained, current observations cannot constrain the two models. However, galaxies at lower stellar masses are being discovered by surveys like the Dark Energy Survey (DES) and HSC-SSP, and potentially hundreds will be found near the Milky Way with the LSST (Tollerud et al. 2008; Walsh et al. 2009; Newton et al. 2018) and out to greater distances using integrated light surveys (Danieli et al. 2018). The masses of the UFDs discovered in DES are highlighted by the gray region in Figure 6. It can be seen that pure number counts of faint dwarfs in LSST (i.e., UFDs found out to $\sim$1 Mpc) can help us to constrain how star formation proceeded at high redshift.

4.3. Satellites of Dwarf Galaxies

As discussed above, the MC simulation contains five times more satellites than the H_2 run at $z = 0$. Here we use this result to estimate the predicted frequency of satellites around dwarfs in the Local Group in the two models.

We follow the methodology in Wheeler et al. (2015) and use the ELVIS suite of collisionless zoom-in simulations of Local-Group-like environments (Garrison-Kimmel et al. 2014) combined with the results of our two simulations to predict the frequency of a satellite around a dwarf galaxy with $M_{\rm vir} \sim 10^{10}$

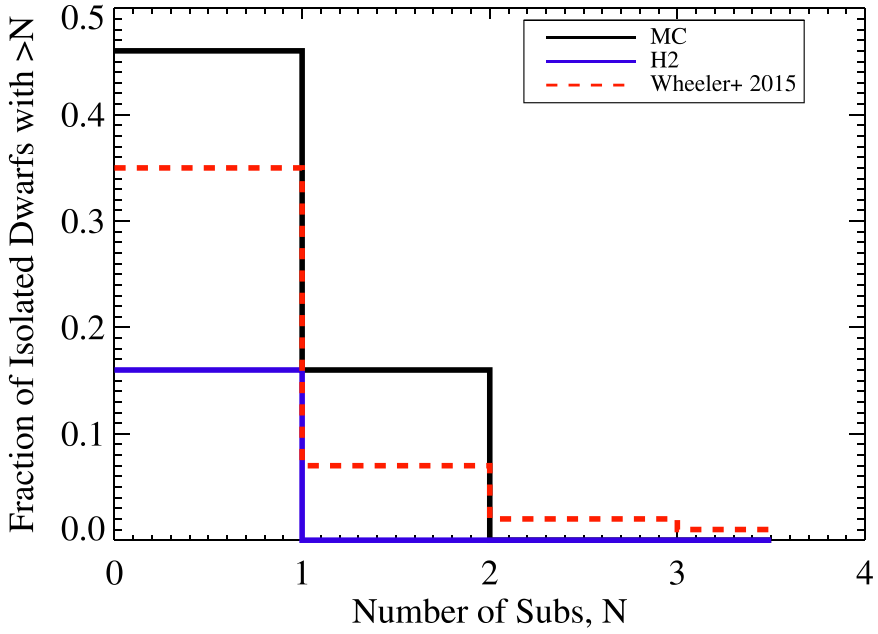

Figure 7. Comparison of the predictions from hydrodynamic simulations for the number of luminous subhalos around dwarf galaxies. The two solid lines are for the simulations in this work (black = MC model; blue = H_2 model), the red dashed line for Wheeler et al. (2015). Each simulation has a different star formation and/or feedback recipe, with the model in Wheeler et al. (2015) being more similar to the MC run (discussed further in the text). This figure demonstrates that the subgrid physics of the simulation affects the predictions for luminous subhalos, in some cases by a factor of ∼4.

$M_\odot$. To summarize the procedure, (1) we select isolated dwarf galaxies from the ELVIS suite from both the isolated and paired Milky-Way-mass halo simulations, and (2) we estimate the frequency of subhalos with peak $M_{\rm vir} \geqslant 10^8\,M_\odot$ within 50 kpc of the dwarf host. Figure 7 shows the results.

As expected, the MC model predicts that UFD satellites of dwarf galaxies are more abundant than the H_2 model. The MC run produces non-negligible frequencies for finding at least one satellite around a dwarf host, 46%. The H_2 model predictions are roughly a factor of 4 lower, at 16%. The H_2 model also suppresses galaxy formation to the point that no Local Group dwarf with $M_{\rm vir} \sim 10^{10}\,M_\odot$ is expected to host more than one luminous satellite companion, while multiple UFD satellites are possible in the MC run.

The Wheeler et al. (2015) results adopt the FIRE 1 star formation and feedback prescription (Hopkins et al. 2014). FIRE 1 adopted a threshold for star formation of $>100\,m_{\rm H}\,{\rm cm}^{-3}$, while the updated FIRE 2 adopts a higher density threshold of $>1000\,m_{\rm H}\,{\rm cm}^{-3}$ (Hopkins et al. 2018). Both FIRE 1 and FIRE 2 use the equilibrium model from Krumholz & Gnedin (2011) to determine the H_2 fraction in a given particle, which is used to calculate the self-shielding of the gas particle and the cooling rate. The presence of H_2 for star formation is an explicit requirement, which is usually ensured by the simultaneous requirement of a high density threshold. However, because FIRE adopts the equilibrium model of H_2, there is no delay in star formation due to the H_2 formation time.

Figure 7 demonstrates that the predictions in Wheeler et al. (2015) are closer to our MC results than H_2 results. This is in line with our expectations given the similarity in star formation threshold (and resolution) between the FIRE 1 model and the MC model. Of course, both the feedback and reionization models in FIRE are different from those used here, which may also play some role in the results. We note, though, that we have adopted a reionization model (Haardt & Madau 2012) that is known to lead to earlier reionization than that used in FIRE (Faucher-Giguère et al. 2009), as was shown in Oñorbe et al. (2017). Despite the stronger, earlier heating in our MC model, we predict slightly more satellites than Wheeler et al. (2015).

The results presented in Figure 7 serve to underscore that current predictions for the number of UFD satellites expected around Local Group dwarfs should be approached with caution. This work highlights the range of values we expect to see in state-of-the-art zoom simulations that reach the UFD mass/luminosity range.[9] However, we do not currently know what star formation physics model is "correct." Until future observations better constrain the models, we must find independent constraints from existing observations.

5. Discussion

In this work, we have found that there is a significant delay in star formation and reduction in overall efficiency of star formation in simulated UFD galaxies when adopting a nonequilibrium H_2-based star formation prescription relative to a prescription that adopts a commonly used temperature–density threshold. We verified that the LW flux external to the galaxies in our H_2 model (due to either the UV background or nearby star-forming galaxies) is not high enough to dissociate H_2 in the halos that fail to form stars. Rather, the reduction in star formation in the H_2 model is due to the long formation times of H_2 at low metallicities in low-mass halos. The delay in H_2 formation prevents or suppresses star formation in UFD galaxies because reionization can heat their gas before significant star formation can occur. In contrast, the MC model allows star formation to occur as soon as gas reaches a high enough density threshold, and more stars form before reionization can remove the gas.

[9] However, we note that these results are all currently based off of simulations of classical field dwarfs, and no one has yet simulated UFDs around a Milky-Way-mass galaxy in a cosmological context.

5.1. Limitations of the Simulations

It is unlikely that either of the explored models, MC or H_2, is "correct." The MC model does not take into account whether the gas can shield when forming stars, and shielding of the gas is likely to be a necessary ingredient for star formation to occur. Similarly, it has been argued that H_2 is not necessary for star formation, but that its presence is correlated with the ability of the gas to shield (Krumholz et al. 2011; Glover & Clark 2012; Krumholz 2012; Mac Low & Glover 2012; Clark & Glover 2014). Hence, it is possible that neither model accurately reflects the physics of star formation in the first halos. Instead, a model that links star formation to shielding may be more appropriate (Byrne et al. 2019).

We emphasize that not all H_2 models for star formation will behave in the same way as our adopted nonequilibrium H_2 model. As discussed throughout this paper, some H_2 models assume equilibrium between the formation and destruction of H_2 in the interstellar medium. Because H_2 formation is not explicitly followed, there will be no dependence on the formation time of H_2 in equilibrium models. Thus, equilibrium H_2 models may behave more like the MC model, though this remains to be tested.

5.1.1. Resolution

As seen in Equation (2), the timescale for H_2 formation is density dependent. Resolution will limit the maximum densities that we are capable of reaching. Figure 4 shows that our dwarf galaxies in the H_2 run that are able to form stars are able to reach gas densities of 1000–$10^5\,m_{\rm H}\,{\rm cm}^{-3}$. Because lower-mass halos will contain fewer gas particles (i.e., fewer resolution elements), this limits their ability to reach the same high densities. Thus, it is possible that some stars should be forming in our dark halos, but that we are unable to capture the process.

However, resolution is a limitation of all simulations, and our goal here is not to present the H_2 model as correct. If we are missing star formation in lower-mass halos, then we would recommend that simulators adopt a model that does not suppress star formation given their resolution (e.g., an equilibrium H_2 model, or a temperature/density threshold model).

It is not clear, though, that we are missing star formation in lower-mass halos. Our H_2 model suppresses star formation in halos below $10^{8.5}\,M_\odot$, and there is no indication to date that this is contrary to observations. Jethwa et al. (2018) used abundance matching to put a lower limit on the peak halo masses of Milky Way UFDs of $>2.4\times10^8\,M_\odot$. Meanwhile, Tollerud & Peek (2018) suggest that reionization prevents galaxy formation in halos below $3\times10^8\,M_\odot$ in peak halo mass. Their model is simple, with a sharp transition that has all halos hosting galaxies above this mass and none below it. This behavior is actually quite similar to our H_2 model. Thus, both of our models are in reasonable agreement with current observational data.

5.1.2. Reionization Model

Many of our low-mass halos in the H_2 model are not able to form stars before reionization prevents them from doing so. Hence, our results may be sensitive to reionization model. Reionization is expected to leave a visible imprint on the satellite luminosity function in the UFD range (Bose et al. 2018). We have adopted the same model in both simulations, following Haardt & Madau (2012). However, Haardt & Madau (2012) have been shown to heat the intergalactic medium earlier ($z\sim15$) than it should (Oñorbe et al. 2017), making the impact of reionization particularly strong on our results. We have left it to future work to quantify the impact of a gentler reionization model on the formation of UFD galaxies and restrict the focus of this paper to the role of star formation recipe alone.

However, the main limitation of our reionization model is the fact that it is uniform throughout the simulation volume. This is common for cosmological galaxy simulations, as the radiative transfer required to explicitly follow patchy reionization is too computationally expensive (and, as noted in Section 2, these runs already cost millions of CPU hours each). Our dwarf volumes are ∼5 Mpc away from a Milky-Way-mass galaxy, meaning that they may be in a lower-density region that was not ionized as early as the higher-density regions surrounding massive galaxies. A more realistic reionization model for this region may then allow some of our dark halos to form stars. The early reionization of Haardt & Madau (2012) may be a better representation of what subhalos that fell into the Milky Way at early times experienced. Because the goal of UFD modeling is often to make predictions for LSST, a model somewhere between the two extremes of late and early reionization is probably more appropriate. However, an accurate study will require radiative transfer to follow the flux of LW radiation and the dissociation of H_2.

5.2. Magellanic Cloud Satellites

Recently, the DES has nearly doubled the number of known UFDs in the Milky Way (Bechtol et al. 2015; Drlica-Wagner et al. 2015; Kim & Jerjen 2015; Kim et al. 2015; Koposov et al. 2015; Luque et al. 2017). Many of the DES dwarfs are thought to potentially be satellites of the Magellanic Cloud system (Deason et al. 2015; Yozin & Bekki 2015; Jethwa et al. 2016; Sales et al. 2017; Kallivayalil et al. 2018; Li et al. 2018). We note that we do not have an LMC-mass galaxy in this simulation volume. The halo mass of the LMC is estimated to be at least $M_{\rm halo}>10^{11}\,M_\odot$ (Besla 2015; Peñarrubia et al. 2016; Dooley et al. 2017a; Erkal et al. 2018; Laporte et al. 2018). A lot of work has been done recently to determine whether the DES dwarfs are satellites of the LMC or Magellanic System (e.g., Deason et al. 2015; Jethwa et al. 2016; Sales et al. 2017). The majority of studies find that 25%–50% of the newly discovered DES dwarfs are likely to have come in with the Magellanic Clouds. Kallivayalil et al. (2018) and Pace & Li (2018) derive proper motions from *Gaia* data to test whether the UFD satellites have kinematics consistent with falling in with the Magellanic Clouds. Between the two studies, seven UFDs are thought to be associated. It is not immediately clear whether these high numbers are compatible with our predictions, given our lack of LMC-mass galaxies.

The models of Dooley et al. (2017a) predict ∼5–15 UFDs with $M_{\rm star}>3000\,M_\odot$ (the lower limit for at least seven star particles in our well-matched galaxy sample) around an LMC-mass galaxy and ∼2–9 around an SMC-mass galaxy. These results are consistent with the number of UFDs that are potentially associated with the Magellanic Cloud system. However, the abundance matching results of Dooley et al. (2017b) put the SMC in a halo with $M_{\rm halo}>10^{11}\,M_\odot$, more massive than our most massive simulated galaxy. Based on

their abundance matching results, a more direct comparison of our most massive simulated galaxies is to WLM, for which Dooley et al. (2017b) expect to find roughly one UFD companion. This suggests that our results are generally consistent with the estimates in Dooley et al. (2017a, 2017b), as they should be as long as our simulation results are reasonably described by one of the SMHM relations that they explore. However, it is unlikely that even our MC model would predict seven satellite companions around an LMC-mass galaxy. To reach such high numbers, the satellites must be associated with the whole Magellanic system (SMC+LMC), rather than just the LMC.

6. Summary

In this work, we have used the highest-resolution simulations to date of a cosmic volume of dwarf galaxies in order to examine the effect of star formation recipes on the formation of UFDs. We run our volume with two different star formation recipes that are common in the literature: one with a temperature/density threshold for star formation, and another that requires the presence of H_2 for star formation. The main differences that manifest between the two models occur in extremely low metallicity gas and are (1) the timescale over which star formation takes place and (2) the effective gas densities at which star particles form (the first above $100\,m_{\rm H}\,{\rm cm}^{-3}$ and the H_2 primarily above $1000\,m_{\rm H}\,{\rm cm}^{-3}$ owing to gravitational collapse during H_2 formation and reduced dust shielding). We find that these differences lead to drastically different results for galaxy formation in halos with $M_{\rm vir} < 10^9\,M_{\odot}$.

Broadly, the ability of the stars in the MC model to form earlier leads to more galaxies that can form in low-mass halos. When the H_2 dependency is introduced into the star formation model, however, gas in low-metallicity, low-mass halos is less likely to reach significant molecular fractions prior to reionization, and gas may never reach densities high enough for dust shielding to allow for substantial H_2. As a result, many fewer low-mass halos in the H_2 run produce stars. Even when they do produce stars, they form substantially less than their matched counterparts in the MC run, leading to a steeper SMHM relation and shallower faint-end SMF.

For the two models that we examine here, we find that twice as many resolved galaxies form in the lower threshold (MC) run. However, most of these are satellites. We also find that more satellites *survive* in the MC run, and we conjecture that feedback in the satellites somehow contributes to the delayed mergers/disruption of these satellites. The combined effect leads to five times as many satellites in the MC run than in the H_2 run.

We have convolved our results with the halos in the ELVIS simulation suite (Garrison-Kimmel et al. 2014) in order to make predictions for the number of UFD satellites around Local Group dwarf galaxies. We find that the MC model predicts that four times as many dwarfs should host at least one luminous satellite compared to the H_2 model, while the H_2 model predicts that no Local Group dwarfs should host more than one UFD satellite. Our MC model produces a similar prediction to that of Wheeler et al. (2015), where the density threshold for star formation was also $100\,m_{\rm H}\,{\rm cm}^{-3}$.

Our goal in this paper is not to figure out which model is correct. Rather, our goal is to stress the need for caution in interpreting simulated UFD results. As simulations push to ever-higher resolution and UFDs begin to be modeled for the first time in fully cosmological simulations run to $z = 0$, the predictions for UFDs are likely to vary from model to model owing to the assumptions adopted by varying modelers. This is in contrast to model predictions in the classical dwarf galaxy mass range because classical dwarf galaxies are capable of self-regulating their star formation, reducing dependency on the adopted prescriptions in their resulting stellar masses. As we push into the UFD mass range, we are simulating galaxies for the first time that can no longer self-regulate.

However, we have highlighted a few future observables that will help to pinpoint the conditions for star formation in the first low-mass halos. Specifically, we have shown that the SMF and the number of UFD satellites around classical dwarf galaxies will be strongly impacted by star formation in UFDs during the reionization epoch. The predicted SMF that can be probed by LSST is shallower in the UFD range for the model that restricts star formation to gas that has H_2. This suggests that pure number counts of UFDs that we discover in the future can help to pinpoint the conditions required for the first star formation in low-mass halos. A better constraint on the slope and scatter of the SMHM relation at low masses will also help to constrain the models.

The authors would like to thank Sarah Loebman, Jillian Bellovary, and Dan Weisz for useful discussions relating to this paper. F.D.M. acknowledges funding from the VIDA fellowship. A.M.B. and F.D.M. acknowledge support from HST-AR-13925. A.M.B. acknowledges support from NSF-AST-1813871. Resources supporting this work were provided by the NASA High-End Computing (HEC) Program through the NASA Advanced Supercomputing (NAS) Division at Ames Research Center. E.A. acknowledges support from the National Science Foundation (NSF) Blue Waters Graduate Fellowship. This research is part of the Blue Waters sustained-petascale computing project, which is supported by the National Science Foundation (awards OCI-0725070 and ACI-1238993) and the state of Illinois. Blue Waters is a joint effort of the University of Illinois at Urbana-Champaign and its National Center for Supercomputing Applications. This work was supported by a PRAC allocation NSF award no. OCI-1144357.

ORCID iDs

Ferah Munshi https://orcid.org/0000-0002-9581-0297
Alyson M. Brooks https://orcid.org/0000-0002-0372-3736
Charlotte Christensen https://orcid.org/0000-0001-6779-3429
Kelly Holley-Bockelmann https://orcid.org/0000-0003-2227-1322

References

Agertz, O., & Kravtsov, A. V. 2016, ApJ, 824, 79
Agertz, O., Kravtsov, A. V., Leitner, S. N., & Gnedin, N. Y. 2013, ApJ, 770, 25
Anderson, L., Governato, F., Karcher, M., Quinn, T., & Wadsley, J. 2017, MNRAS, 468, 4077
Arraki, K. S., Klypin, A., More, S., & Trujillo-Gomez, S. 2014, MNRAS, 438, 1466
Aumer, M., White, S. D. M., Naab, T., & Scannapieco, C. 2013, MNRAS, 434, 3142
Barnes, J., & Efstathiou, G. 1987, ApJ, 319, 575
Bechtol, K., Drlica-Wagner, A., Balbinot, E., et al. 2015, ApJ, 807, 50

Benincasa, S. M., Wadsley, J., Couchman, H. M. P., & Keller, B. W. 2016, MNRAS, 462, 3053
Besla, G. 2015, arXiv:1511.03346
Booth, C. M., Agertz, O., Kravtsov, A. V., & Gnedin, N. Y. 2013, ApJL, 777, L16
Bose, S., Deason, A. J., & Frenk, C. S. 2018, ApJ, 863, 123
Brook, C. B., Di Cintio, A., Knebe, A., et al. 2014, ApJL, 784, L14
Brook, C. B., Governato, F., Roškar, R., et al. 2011, MNRAS, 415, 1051
Brook, C. B., Stinson, G., Gibson, B. K., Wadsley, J., & Quinn, T. 2012, MNRAS, 424, 1275
Brooks, A. M., Governato, F., Booth, C. M., et al. 2007, ApJL, 655, L17
Brooks, A. M., Papastergis, E., Christensen, C. R., et al. 2017, ApJ, 850, 97
Brooks, A. M., Solomon, A. R., Governato, F., et al. 2011, ApJ, 728, 51
Brooks, A. M., & Zolotov, A. 2014, ApJ, 786, 87
Brown, T. M., Tumlinson, J., Geha, M., et al. 2012, ApJL, 753, L21
Brown, T. M., Tumlinson, J., Geha, M., et al. 2014, ApJ, 796, 91
Buck, T., Dutton, A. A., & Macciò, A. V. 2018, arXiv:1812.05613
Byrne, L., Christensen, C., Tsekitsidis, M., Brooks, A., & Quinn, T. 2019, arXiv:1901.00864
Carlin, J. L., Sand, D. J., Price, P., et al. 2016, ApJL, 828, L5
Christensen, C., Quinn, T., Governato, F., et al. 2012, MNRAS, 425, 3058
Christensen, C. R., Brooks, A. M., Fisher, D. B., et al. 2014a, MNRAS, 440, L51
Christensen, C. R., Davé, R., Governato, F., et al. 2016, ApJ, 824, 57
Christensen, C. R., Governato, F., Quinn, T., et al. 2014b, MNRAS, 440, 2843
Clark, P. C., & Glover, S. C. O. 2014, MNRAS, 444, 2396
Corlies, L., Johnston, K. V., & Wise, J. H. 2018, MNRAS, 475, 4868
Danieli, S., van Dokkum, P., & Conroy, C. 2018, ApJ, 856, 69
D'Onghia, E., & Lake, G. 2008, ApJL, 686, L61
Deason, A. J., Wetzel, A. R., Garrison-Kimmel, S., & Belokurov, V. 2015, MNRAS, 453, 3568
Diemand, J., Madau, P., & Moore, B. 2005, MNRAS, 364, 367
Dooley, G. A., Peter, A. H. G., Carlin, J. L., et al. 2017a, MNRAS, 472, 1060
Dooley, G. A., Peter, A. H. G., Yang, T., et al. 2017b, MNRAS, 471, 4894
Drlica-Wagner, A., Bechtol, K., Rykoff, E. S., et al. 2015, ApJ, 813, 109
Erkal, D., Belokurov, V., Laporte, C. F. P., et al. 2018, arXiv:1812.08192
Farber, R., Ruszkowski, M., Yang, H.-Y. K., & Zweibel, E. G. 2018, ApJ, 856, 112
Fattahi, A., Navarro, J. F., Sawala, T., et al. 2016, MNRAS, 457, 844
Faucher-Giguère, C.-A., Lidz, A., Zaldarriaga, M., & Hernquist, L. 2009, ApJ, 703, 1416
Fitts, A., Boylan-Kolchin, M., Elbert, O. D., et al. 2017, MNRAS, 471, 3547
Fry, A. B., Governato, F., Pontzen, A., et al. 2015, MNRAS, 452, 1468
Garrison-Kimmel, S., Boylan-Kolchin, M., Bullock, J. S., & Lee, K. 2014, MNRAS, 438, 2578
Garrison-Kimmel, S., Bullock, J. S., Boylan-Kolchin, M., & Bardwell, E. 2017a, MNRAS, 464, 3108
Garrison-Kimmel, S., Hopkins, P. F., Wetzel, A., et al. 2018, arXiv:1806.04143
Garrison-Kimmel, S., Wetzel, A., Bullock, J. S., et al. 2017b, MNRAS, 471, 1709
Gill, S. P. D., Knebe, A., & Gibson, B. K. 2004, MNRAS, 351, 399
Glover, S. C. O., & Clark, P. C. 2012, MNRAS, 421, 116
Gnedin, N. Y., & Kravtsov, A. V. 2010, ApJ, 714, 287
Gnedin, N. Y., & Kravtsov, A. V. 2011, ApJ, 728, 88
Gnedin, N. Y., Tassis, K., & Kravtsov, A. V. 2009, ApJ, 697, 55
Governato, F., Brook, C., Mayer, L., et al. 2010, Natur, 463, 203
Governato, F., Zolotov, A., Pontzen, A., et al. 2012, MNRAS, 422, 1231
Haardt, F., & Madau, P. 2012, ApJ, 746, 125
Homma, D., Chiba, M., Okamoto, S., et al. 2018, PASJ, 70, S18
Hopkins, P. F., Kereš, D., Oñorbe, J., et al. 2014, MNRAS, 445, 581
Hopkins, P. F., Narayanan, D., & Murray, N. 2013, MNRAS, 432, 2647
Hopkins, P. F., Quataert, E., & Murray, N. 2011, MNRAS, 417, 950
Hopkins, P. F., Quataert, E., & Murray, N. 2012, MNRAS, 421, 3522
Hopkins, P. F., Wetzel, A., Kereš, D., et al. 2018, MNRAS, 480, 800
Jeon, M., Besla, G., & Bromm, V. 2017, ApJ, 848, 85
Jethwa, P., Erkal, D., & Belokurov, V. 2016, MNRAS, 461, 2212
Jethwa, P., Erkal, D., & Belokurov, V. 2018, MNRAS, 473, 2060
Kallivayalil, N., Sales, L., Zivick, P., et al. 2018, arXiv:1805.01448
Kannan, R., Marinacci, F., Simpson, C. M., Glover, S. C. O., & Hernquist, L. 2018, ApJ, 867, 19
Katz, N., & White, S. D. M. 1993, ApJ, 412, 455
Kim, D., & Jerjen, H. 2015, ApJL, 808, L39
Kim, D., Jerjen, H., Mackey, D., Da Costa, G. S., & Milone, A. P. 2015, ApJL, 804, L44
Kim, J.-h., Abel, T., Agertz, O., et al. 2014, ApJS, 210, 14
Kim, J.-h., Agertz, O., Teyssier, R., et al. 2016, ApJ, 833, 202
Knollmann, S. R., & Knebe, A. 2009, ApJS, 182, 608
Koposov, S. E., Belokurov, V., Torrealba, G., & Evans, N. W. 2015, ApJ, 805, 130
Krumholz, M. R. 2012, ApJ, 759, 9
Krumholz, M. R., & Gnedin, N. Y. 2011, ApJ, 729, 36
Krumholz, M. R., Leroy, A. K., & McKee, C. F. 2011, ApJ, 731, 25
Krumholz, M. R., McKee, C. F., & Tumlinson, J. 2008, ApJ, 689, 865
Krumholz, M. R., McKee, C. F., & Tumlinson, J. 2009, ApJ, 693, 216
Kuhlen, M., Krumholz, M. R., Madau, P., Smith, B. D., & Wise, J. 2012, ApJ, 749, 36
Kuhlen, M., Madau, P., & Krumholz, M. R. 2013, ApJ, 776, 34
Laporte, C. F. P., Gómez, F. A., Besla, G., Johnston, K. V., & Garavito-Camargo, N. 2018, MNRAS, 473, 1218
Li, T. S., Simon, J. D., Pace, A. B., et al. 2018, ApJ, 857, 145
Li, Y.-S., & Helmi, A. 2008, MNRAS, 385, 1365
Lin, W., & Ishak, M. 2016, JCAP, 10, 025
Luque, E., Pieres, A., Santiago, B., et al. 2017, MNRAS, 468, 97
Mac Low, M.-M., & Glover, S. C. O. 2012, ApJ, 746, 135
McConnachie, A. W. 2012, AJ, 144, 4
Menon, H., Wesolowski, L., Zheng, G., et al. 2015, ComAC, 2, 1
Munshi, F., Brooks, A. M., Applebaum, E., et al. 2017, arXiv:1705.06286
Munshi, F., Governato, F., Brooks, A. M., et al. 2013, ApJ, 766, 56
Murray, N., Ménard, B., & Thompson, T. A. 2011, ApJ, 735, 66
Nelson, D., Pillepich, A., Springel, V., et al. 2018, MNRAS, 475, 624
Newton, O., Cautun, M., Jenkins, A., Frenk, C. S., & Helly, J. C. 2018, MNRAS, 479, 2853
Nichols, M., Colless, J., Colless, M., & Bland-Hawthorn, J. 2011, ApJ, 742, 110
Oñorbe, J., Boylan-Kolchin, M., Bullock, J. S., et al. 2015, MNRAS, 454, 2092
Oñorbe, J., Hennawi, J. F., & Lukić, Z. 2017, ApJ, 837, 106
Pace, A. B., & Li, T. S. 2018, arXiv:1806.02345
Pallottini, A., Ferrara, A., Bovino, S., et al. 2017, MNRAS, 471, 4128
Patel, E., Carlin, J. L., Tollerud, E. J., Collins, M. L. M., & Dooley, G. A. 2018, MNRAS, 480, 1883
Peñarrubia, J., Benson, A. J., Walker, M. G., et al. 2010, MNRAS, 406, 1290
Peñarrubia, J., Gómez, F. A., Besla, G., Erkal, D., & Ma, Y.-Z. 2016, MNRAS, 456, L54
Pontzen, A., Governato, F., Pettini, M., et al. 2008, MNRAS, 390, 1349
Rashkov, V., Madau, P., Kuhlen, M., & Diemand, J. 2012, ApJ, 745, 142
Read, J. I., Agertz, O., & Collins, M. L. M. 2016, MNRAS, 459, 2573
Read, J. I., Iorio, G., Agertz, O., & Fraternali, F. 2017, MNRAS, 467, 2019
Robertson, B. E., & Kravtsov, A. V. 2008, ApJ, 680, 1083
Saitoh, T. R., Daisaka, H., Kokubo, E., et al. 2008, PASJ, 60, 667
Salem, M., Bryan, G. L., & Corlies, L. 2016, MNRAS, 456, 582
Sales, L. V., Navarro, J. F., Cooper, A. P., et al. 2011, MNRAS, 418, 648
Sales, L. V., Navarro, J. F., Kallivayalil, N., & Frenk, C. S. 2017, MNRAS, 465, 1879
Sales, L. V., Wang, W., White, S. D. M., & Navarro, J. F. 2013, MNRAS, 428, 573
Santos-Santos, I. M., Di Cintio, A., Brook, C. B., et al. 2018, MNRAS, 473, 4392
Sawala, T., Frenk, C. S., Crain, R. A., et al. 2013, MNRAS, 431, 1366
Sawala, T., Frenk, C. S., Fattahi, A., et al. 2015, MNRAS, 448, 2941
Sawala, T., Frenk, C. S., Fattahi, A., et al. 2016, MNRAS, 457, 1931
Schaye, J., Crain, R. A., Bower, R. G., et al. 2015, MNRAS, 446, 521
Schewtschenko, J. A., & Macciò, A. V. 2011, MNRAS, 413, 878
Semenov, V. A., Kravtsov, A. V., & Gnedin, N. Y. 2016, ApJ, 826, 200
Semenov, V. A., Kravtsov, A. V., & Gnedin, N. Y. 2018, ApJ, 861, 4
Sharma, M., & Nath, B. B. 2012, ApJ, 750, 55
Shen, S., Madau, P., Conroy, C., Governato, F., & Mayer, L. 2014, ApJ, 792, 99
Shen, S., Wadsley, J., & Stinson, G. 2010, MNRAS, 407, 1581
Simpson, C. M., Pakmor, R., Marinacci, F., et al. 2016, ApJL, 827, L29
Sternberg, A., Le Petit, F., Roueff, E., & Le Bourlot, J. 2014, ApJ, 790, 10
Stinson, G., Seth, A., Katz, N., et al. 2006, MNRAS, 373, 1074
Stinson, G. S., Bailin, J., Couchman, H., et al. 2010, MNRAS, 408, 812
Thompson, T. A., Quataert, E., & Murray, N. 2005, ApJ, 630, 167
Tollerud, E. J., Bullock, J. S., Strigari, L. E., & Willman, B. 2008, ApJ, 688, 277
Tollerud, E. J., & Peek, J. E. G. 2018, ApJ, 857, 45
Tremmel, M., Karcher, M., Governato, F., et al. 2017, MNRAS, 470, 1121
Vogelsberger, M., Genel, S., Sijacki, D., et al. 2013, MNRAS, 436, 3031
Wadsley, J. W., Keller, B. W., & Quinn, T. R. 2017, MNRAS, 471, 2357

Walsh, S. M., Willman, B., & Jerjen, H. 2009, AJ, 137, 450
Wang, L., Dutton, A. A., Stinson, G. S., et al. 2015, MNRAS, 454, 83
Weisz, D. R., Dolphin, A. E., Skillman, E. D., et al. 2014a, ApJ, 789, 147
Weisz, D. R., Dolphin, A. E., Skillman, E. D., et al. 2014b, ApJ, 789, 148
Wheeler, C., Hopkins, P. F., Pace, A. B., et al. 2018, arXiv:1812.02749
Wheeler, C., Oñorbe, J., Bullock, J. S., et al. 2015, MNRAS, 453, 1305
Wise, J. H., Abel, T., Turk, M. J., Norman, M. L., & Smith, B. D. 2012, MNRAS, 427, 311
Wright, A. C., Brooks, A. M., Weisz, D. R., & Christensen, C. R. 2019, MNRAS, 482, 1176
Yozin, C., & Bekki, K. 2015, MNRAS, 453, 2302
Zolotov, A., Brooks, A. M., Willman, B., et al. 2012, ApJ, 761, 71